UCRL - 76210 Rev 1
PREPRINT
Conf-741105--55

LAWRENCE LIVERMORE LABORATORY
University of California / Livermore, California

LASER PLASMA EXPERIMENTS RELEVANT TO LASER PRODUCED IMPLOSIONS

H. G. Ahlstrom, J. F. Holzrichter, K. R. Manes,
L. W. Coleman, D. R. Speck, R. A. Haas, and H. D. Shay

November 7, 1974

This Paper Was Prepared For Submission To
The Fifth Conference On
Plasma Physics and Controlled Nuclear Fusion Research
Tokyo, Japan - November 11-15, 1974

LASER PLASMA EXPERIMENTS RELEVANT TO LASER PRODUCED IMPLOSIONS*

H. G. Ahlstrom, J. F. Holzrichter, K. P. Manes,
L. W. Coleman, T. R. Speck, P. A. Haas, and H. D. Shay
Lawrence Livermore Laboratory, University of California
Livermore, California 94550

November 7, 1974

ABSTRACT

Preliminary laser target interaction studies designed to provide code normalization data in a regime of interest to laser fusion are reported. The laser facilities constructed for such studies, the target diagnostic systems, and preliminary experimental results are described.

*Work performed under the auspices of the U. S. Atomic Energy Commission.

I. INTRODUCTION

The laser target interaction program at LLL has as its major goal the attainment of "breakeven" fusion. The primary facility for pursuing breakeven experiments will be a multiple beam 1.06 μm system named SHIVA which has been designed to produce 10 kJ in 500 psec and is due for completion in 1977. For preliminary laser target experimentation, three small laser target facilities have been constructed. The most powerful of these is a two beam 1.06 μm laser system, Janus, which can deliver up to 40 J from each arm to a target in 100 psec. A CO_2 laser system, Valkyrie, irradiates targets with 1 nsec duration 10.6 μm pulses containing 50 J. In addition, the Livermore Long Path Laser which is capable of 50 J in 1 to 3 nsec has been used for preliminary experiments. Other intermediate facilities (1 kJ energy at 1.06 μm are being constructed and will be operational in 12 months. These devices will employ the techniques and hardware tested by Livermore's single beam developmental laser system, Cyclops, which has produced 270 J in 150 psec.

The immediate goal of the LLL experimental program is to provide accurate experimental information on which to base extended theoretical calculations. Initial experiments have been concerned with laser target coupling to foil and bulk targets, including measurements of shock wave development. It has not been assumed a priori that the laser systems or the targets will necessarily behave in a reproducible manner. Extensive measurements on the time history, spatial distribution, spectral content, and focusing characteristics of the incident, forward scattered, and back scattered laser light are provided on each shot. The behavior of the

target is monitored by a battery of x-ray spectral measuring devices, electron spectrometers, ion collectors, ultra-fast x-ray and visible streak cameras, and other diagnostic devices which will be discussed in connection with the specific experiments described below.

In the following, the three laser systems dedicated to target interaction studies at LLL are described. Some preliminary experimental results are reported and the performance of some new diagnostic devices is demonstrated.

II. LASER SYSTEMS

A. Janus

The Janus laser system is designed to produce high power 1.06 μm laser radiation for laser fusion experiments. The design specifications are:

50 J per beam (2 beams)

100 psec full width at half max. pulse height

bandwidth limited spectrum

fully isolated from 100% target feedback

The above specifications are being met as the system assembly is completed.

The laser system shown in Fig. 1 and Fig. 2 consists of a dye mode-locked Nd:YAG oscillator, YAG and glass pre amplifiers, and a series of 3.5 cm and 8.5 cm aperture disk amplifiers.[1] The total gain of the system is 10^4. The design minimizes the integral of laser intensity times glass path, $\int I d\ell$, in order to enhance short pulse operation.

After leaving the oscillator the pulse is amplified, spatially filtered and apodized to provide a smooth optimally shaped pulse for amplification in the amplifier chain. The resulting spatial pulse is approximately $e^{-(r/r_o)^5}$ in shape. In the early stages of the amplifier train the beam is truncated beyond 10^{-3} I_{max} to minimize diffraction in the beam. The apodized pulse is amplified in a chain consisting of three 25 mm x 250 mm rod amplifiers, two "A" (35 mm aperture) disk amplifiers each containing 6 15 mm thick brewster angle disks and two

"B" (85 mm aperture) disk amplifiers each containing 6 23.5 mm thick brewster angle disks. After this amplification, the beam energy is up to 40 joules. This beam is either sent to the target chamber along one arm of the amplifier or split into two beams and reamplified with an additional "B" amplifier in each arm to provide the 50 joules/beam output. Faraday rotator isolators are used to stabilize the amplifier system against self-oscillation and against reflection from the laser targets. A dye cell is used to reduce the amplified spontaneous emissions to below 10 mJ at the target.

Extensive diagnostics allow the laser beam to be fully characterized. These diagnostics include an SI streak camera (< 10 nsec resolution), near field and far field variable exposure cameras for beam profile measurements, ballistic calorimeters, and a 50 db dynamic range pre-pulse detection system.

The laser beam is directed into a target chamber where the radiation is focused onto a target. We are presently using an aspheric f/1 lens. Fig. 3 shows the optical diagnostic set-up. A second lens is used to image the focal region onto a TV tube, streak camera, and multiple exposure camera. The imaging system allows very accurate positioning of the laser focal spot with respect to the target typically ±10μ. In addition the focal spot intensity distribution may be viewed directly. Fig. 4 shows the Janus target chamber being readied for fusion experiments.

B. Valkyrie

The Livermore CO_2 laser system, Valkyrie, was constructed to provide an experimental facility capable of delivering 50 J in a diffraction

limited beam at 10.6 μm in 1 nsec. This device has met all of its design goals and is in operation as a target irradiation facility.[1] On a typical day, Valkyrie provides 40 J · 10⁹ in ~1 nsec at a repetition rate limited by the time required to replace targets.

Valkyrie's oscillator, located in the background of Fig. 5, employs a specially designed u-v preionized TEA gain medium (Lumonics 142A), a Ge Brewster's angle acousto-optic mode-locker, and an NaCl etalon as an output mirror. This oscillator generates a burst of 1 nsec duration pulses with peak pulse energies in excess of 50 mJ distributed reproducibly among six rotational lines centered on the P20 transiton of the 10.4 μm band. A single pulse is selected by a switch-out assembly consisting of a laser triggered spark gap and a CdTe Pockel's cell. The pulse is then directed through a second Lumonics 142A which serves as a preamplifier and into a 3 X Keplerian beam expander with a spatial filter at its focus. Expanded and collimated, the pulse propagates through a nine centimeter aperture uv-preionized TEA amplifier (Lumonics 602A) followed by two eleven centimeter aperture cold-cathode e-beam sustained amplifiers operated at two atmospheres. Emerging in the target area, the pulse contains ~50 J in ~1 nsec with an approximately Gaussian spatial intensity distribution. Two NaCl beam-splitters which are wedged and anti-reflection coated with NaF on one face provide diagnostic beams for intensity profile, energy, temporal character and spectral measurements. The main beam is finally focussed to an ~80 μm diameter spot by an f/2 aspheric NaCl lens mounted inside of the spherical vacuum vessel in Fig. 6. Since this laser-target chamber system became

available in September, we have concentrated primarily on assembling and calibrating diagnostics, suppressing parasitic oscillations, and other laser system related problems. Nevertheless, some preliminary data has been accumulated by irradiating ~ 5 μ thick CH_2 foils at the 10^{14} watts/cm^2 level. About 6 ± 1 percent of the incident energy is scattered back into a 0.1 steradian cone centered on the incident beam. Relatively weak forward scattered signals are detected whose amplitude is independent of input energy suggesting that the target foils do not go underdense during the 1 nsec irradiation.

C. Long-Path

The Long-Path Nd:YAG-Glass Laser system performance characteristics have been described in detail previously.[2] Briefly, it consists of an oscillator, a stretched-out chain of rod amplifiers, and a multi-pass disk amplifier. Both rods and disks are made of neodymium doped glass. Measurements of the temporal[3] and spatial[4] output beam pulse shape have revealed significant and irreproducible nonuniformities. Recently, in an effort to improve the performance of the system, the oscillator was replaced with an actively mode locked Nd:YAG oscillator whose cavity bandwidth is controlled with a Fabry-Perot etalon. This new system produces smooth 1 - 3 nsec FWHM, 50 J or less, pulses depending on the oscillator cavity etalon bandwidth and the amplifier chain flash lamp pumping power. However, far field camera pictures of the output pulse indicate that significant spatial modulation remains on the beam. Because of the spatial modulation, the Long-Path Laser has been used to develop and check out plasma diagnostics and for preliminary foil acceleration experiments. Long-Path delivers its pulse to the target chamber shown in Fig. 7.

III. TARGET EXPERIMENTS

A. Plasma Development in Low Z Laser Fusion Targets

In this section two problems associated with the initial stages of target heating by laser radiation are discussed. The first problem is the energy delivered to the target prematurely because of imperfect mode-locking in the laser oscillator and amplified spontaneous emission through the amplifier chain. The second problem is the initiation and the growth of the breakdown of the dielectric material.

To achieve the short pulses required for laser fusion experiments a dye-mode-locked oscillatior is used to generate 100 psec, gaussian pulses. The mode-locking process starts from bandwidth limited, spontaneous fluorescence noise produced by the active oscillator materials.[5] The more intense noise pulses begin to bleach the mode-locking dye as they are amplified during sequential round trips in the optical resonator. The most intense pulse generally wins out and is observed as the mode-locked oscillator output signal. In an actively mode-locked oscillator in the cw limit, only one pulse developes to the steady state limit.[6] In our oscillator, the passive mode-locking procedure and operation in the transient regime may allow lower level noise pulses to appear in the mode-locked pulse train. Parasitic feedback loops often exist in a complicated optical resonator because of dust particles, damage spots, etc. These feedback mechanisms can give rise to pulses in a mode-locked pulse train. Such low level pulses can be amplified to levels which are sufficient to destroy laser fusion targets before the arrival of the main heating pulse.

An additional source of target damage is amplified spontaneous emission (ASE). Target damage occurs when the amplifier gain is sufficient to amplify spontaneous noise generated in the initial stages of the amplifier train to damaging levels. The experiments described here were done on two laser systems at LLL: the JANUS system and the Long Path Laser. A calculation of the expected ASE noise level has been done by Leppelmeier.[7] For the JANUS system, where the amplifier gain at 1.06 μ may be greater than 10^4, 1-20 mJ of energy may be intercepted by the target. This level of irradiation can cause premature target damage.

Understanding premature target damage and the early development of laser plasmas relies on a detailed knowledge of the initial stages of plasma formation. For uniform compression of fusion targets, it is important that the critical density surface developes from the initial breakdown point at a rate that is fast compared to the fluid dynamic rate for the implosion. Present theories of optical damage in solid dielectrics[8] stress the statistical nature of the beginning of an electron avalanche process. Our primary interest is to determine the reproducibility of the breakdown process and the rate of growth of the critical density surface in a direction transverse to the optical axis.

The energy required to exceed typical dielectric breakdown thresholds in laser fusion targets is very small because of their small dimensions. A typical laser fusion target, as shown in Figure 8, may subtend an area of 4×10^{-4} cm^2. Milli-joules of laser energy distributed uniformly over the target produces an energy flux of several J/cm^2; levels which exceed glass dielectric breakdown thresholds.[8] If the target material is not

completely clean or if there are glue spots or dust particles attached to the surface, damage may occur at levels lower than those associated with the intrinsic breakdown limit.

Figure 9a shows a typical damage site on a hollow glass ball which was purposely irradiated with 100 psec, milli-joule energy pulses. Figure 9b shows that more complete damage can occur when the focusing conditions differ. In this case a 100-300 μJ pulse was focused onto the glue joint. This damage, if it developed before the laser compression pulse arrived, would prevent meanful compression of the target.

The absolute short-pulse damage threshold of these glass shell targets has not yet been determined. The optical aberrations of our lenses, as well as the static and dynamic aberrations of the laser systems have prevented accurate measurements of the absolute energy density of the interference structure in the focal region. Our philosophy has been to eliminate any change of target malfunction caused by pre-pulse processes. To this end, fast pockel's cell switches, saturable absorbers, and precise monitoring techniques are under development.

Target damage from amplified spontaneous emission is difficult to quantify. When a target intercepts more than 10 mJ of 1.06 radiation, damage to the glue joints may occur. The damage threshold is very sensitive to the type of glue used and to the orientation of the glue joint with respect to the optical axis. When the ASE damage occurs in time is still unknown. Since the laser pulse usually occurs about half way through the fluorescence pump pulse (about 500 μsec into an 800 μsec flashlamp pulse) it is possible that the target is still intact when the laser compression pulse arrives. Until more data on this point has been gathered the

amplified spontaneous emission level will be reduced below the target damage threshold observed upon inspecting the target after the pump pulse.

The prepulse history of the mode-locked laser oscillator on the JANUS system has been measured over an intensity range of 50 db, with time resolution of 1 nsec. The experimental arrangement is shown in Figure 10. A fiducial pulse is generated by the glass wedges and follows path 1 to allow identification of the single switched-out oscillator pulse, of the residuals from rejected pulses in the train, and of spurious noise pulses. Appropriately placed beam attenuators and the high photodiode sensitivity allow the observation of temporal structure which is up to 50 db down in intensity from the main pulse.

Figure 11 shows some typical results from the JANUS oscillator. Eighteen pulse trains were examined, of these 4 trains had pre-pulse energies less than 30 db down from the main pulse, 8 trains had no structure at all. The residual intensity in the pulse preceeding the switched-out pulse is down at least 50 db.

For the JANUS laser system which is designed to produce 20-40 J pulses, a 40 db reduction in intensity still leaves 2-4 mJ of energy which can damage the target. As a result, we feel that it is very important to carefully tune the oscillator and to monitor each targe pulse. Saturable absorbers are under consideration to further reduce pre-pulse effects.

To study the transverse development of the critical density in a dielectric target, transmitted laser light has been observed as a function of time. Figure 3 shows the experimental set-up. The purpose of this experiment is to set limits on the rate of formation of the critical surface.

Figure 12 shows a streak photograph of the time development of the breakdown. The image of the laser focal regions is seen to increase in intensity until breakdown occurs at the center of the beam. At this point, 1.06 μm radiation is either absorbed at the critical surface or refracted out of the field of view. The transverse rate of plasma formation is given by the growth of the absorbing region. The rate of growth is very dependent on the power delivered to the critical region. While a number is not yet available for this growth rate, an accurate value will be provided shortly.

B. Foil Acceleration Studies

The production of thermonuclear energy by laser driven implosion of large aspect ratio spherical DT shells[9], ((shell radius r/shell thickness Δr) $\sim$ 30 - 50), with achievable laser technology, requires the development of an efficient and fluid dynamically stable implosion. The efficiency is determined, primarily, by the laser-plasma coupling and the mechanism for energy transport from the laser energy absorption region to the shell ablation surface. The large aspect ratio of the target permits the same compression state to be reached, as that required for a solid body, with a smaller driving pressure. Thus, the laser energy can be delivered over a longer time minimizing the laser intensity and concomitant production of high energy electrons by parametric and resonant processes and optimizing the efficient absorption of laser energy by inverse bremsstrahlung. However, fluid dynamic stability considerations place a limit on the aspect ratio. For instance, computer modeling calculations[10] indicate that a Rayleigh-Taylor type instability may occur during the implosion of the shell. If a is the instantaneous acceleration of the shell then the classical growth of a small amplitude perturbation x on the shell's surface is given by

$$x = x_o \exp \int_0^t \frac{1}{2} \frac{at^2}{\Delta r} \frac{dt}{t} \qquad (1)$$

Since the distance moved by the shell in time t is on the order of $at^2/2$, surface perturbations will increase dramatically in amplitude

after the shell has moved a distance of only a few shell thicknesses. In laser driven implosions the fluid dynamic stability is much more complicated and depends on details of the shell acceleration and ablation process that are not yet well understood.

With the exception of the spherical convergence, the efficiency and stability of the acceleration of spherical shells can be studied experimentally by irradiating thin, 5-25 μm thick, polyethylene foils and disks with 50-100 J, 1.06 μm wavelength, laser light pulses whose durations are .1-1 nsec. This section reports preliminary results of foil acceleration experiments obtained using the Long Path Nd:YAG-glass laser system. In the following the details of the experimental program are presented and preliminary results discussed and compared to theoretical predictions. No effort has been made to model these results in detail due to the preliminary nature of the data. The focal spot spatial distribution of the laser energy for this laser is too irregular to provide definitive experimental data. For instance, it is difficult to distinguish between fluid dynamic instability effects and effects due to irregularities in the spatial distribution of the laser energy deposition. To solve this problem these experiments will soon be carried out on two new laser systems: JANUS and Valkyrie. Both of these lasers produce the refined, well characterized pulses required in these experiments.

The targets employed in these experiments fall into two catagories; (1) 5-25 μm thick polyethylene foils and (2) 10-25 μm thick by 20-300 μm diameter polyethylene disks (microdots) that have been deposited on a 500 Å thick parylene foil. As indicated in Figure 13, these foils are supported by low Z metal frames, such as Beryllium and Aluminum, whose thickness,

inside and outside diameters are nominally: .8 mm, .5 cm and 1.0 cm, respectively. Due to the possibility of fluid dynamic instability, the surface quality of the target is a property of considerable importance. Suppose the shell mass accelerates as a $\sim t^m$ for a distance $x \sim 50\ \Delta x$. Then in order to prevent penetration of the shell by surface perturbations that grow at the calssical Rayleigh-Taylor rate the initial surface perturbations x_o must be such that: $x_o < .0062\ \Delta x$ for $m = 0$ and $x_o < .0085\ \Delta x$ for $m \to \infty$. The targets employed in the present experiments do not satisfy these flatness conditions. However, targets with very smooth surfaces are under development.

Although the polyethylene foils are easier to make they have several severe limitations. The role of boundary conditions at the interface between the accelerated low temperature plasma and the cold foil is difficult to assess. For instance, the laser light refracted by the blowoff plasma, which acts as a negative lens, is absorbed by the cold foil near the accelerated matter complicating the dynamics of the system and preventing crucial energy balance measurements. In addition, two dimensional calculations, performed using the LASNEX computer code,[11] indicate that if the laser energy distribution across the target foil varies too rapidly a high velocity shear region appears between the cold foil and the accelerated low temperature plasma. This velocity shear region can exhibit Kelvin-Helmholtz instability. When this happens the rapid growth of the instability grossly distorts the edges of the accelerated matter complicating the interpretation of the experimental results.

The microdot targets are being developed to circumvent these difficulties.

The thickness of the parylene foil is such that the energy and time required to destroy the foil are both small compared to the incident laser pulse energy and time, respectively. The design of the experiment then requires that the laser pulse energy distribution across the target and the target diameter be such that over most of the target the acceleration physics is nearly one-dimensional. For uniform irradiation, the target motion is nearly one-dimensional if its diameter is much greater than the transverse electron thermal conduction length and the time scale of the event is much less than the acoustic transit time through the cool accelerated matter. For the present experiments this requires the diameter of the target to be greater than two hundred microns.

The LASNEX computer code, written by George Zimmerman, has been used to design experiments and study the physics of the foil acceleration. In the experiments reported here the laser intensity is above the threshold intensity

$$I_{th} \quad (w/cm^2) \simeq \left(\frac{10^{-45}}{T_e} \right) n_c^3 S \left(\frac{\bar{Z}^2}{\bar{I}} \right)^2 \qquad (2)$$

for parametric instability absorption. where the swelling factor $S^{-1} = 3.6 \left(\frac{2\pi L}{\lambda_0} \right)^{1/3}$. The critical electron density, electron temperature, average ion charge and density scale length are n_c, T_e, $\bar{Z}$ and L respectively. Previous comparisons[12] of LASNEX predictions with experimental measurements of the x-ray emission spectra from plasmas produced by irradiation of thick

CH_2 slabs showed good agreement with S ~ 1/20. In general this threshold estimate is crude and does not treat the competing mechanism of suprathermal electron acceleration by resonant absorption. To bracket the possibilities and predict the results expected from the present experiments, two series of calculations were performed assuming: (1) only inverse bremsstrahlung absorption and (2) a parametric instability absorption threshold 1000 times lower than that predicted above.

Figure 14 presents the results of a LASNEX calculation of the plasma mass density and electron temperature evolution for a one-dimensional CH_2 foil acceleration. The foil was initially 10 μm thick. It is being irradiated by a 25 J, 1.4 nsec FWHM Gaussian, 1.06 μm wavelength, laser pulse that has been focused to a 200 μm diameter spot on the foil. In this calculation the peak laser intensity is 1000 times above threshold intensity for parametric instability absorption. Consequently, about 25% of the laser energy produces a superthermal electron distribution of the form

$$f(v) \quad \exp\ (-v^2/12\ kT_e).$$

Part of the absorbed energy is transported by electron thermal conduction to the surface of the foil. Violent ablation and blow off of the surface produces a compression force on the foil thereby driving a shock wave through it. The shock wave heats and compresses the foil to roughly 5-10 ev and 4.5 times solid density, respectively. This early behavior is relatively insensitive to the absorption assumption.

The momentum transferred to the foil due to the ablation of its surface accelerates the foil. Initially after compression by the first shock wave the mass density and temperature, of the foil interior, remain nearly constant. However, as the pulse intensity rises, due to superthermal electron preheat, the foil begins to heat up and disassemble. By the peak

of the laser pulse the foil's maximum density surface has moved 36 μm. Its maximum density has dropped to more than four times below solid density and the back surface of the accelerated plasma has been heated to a temperature of 50 ev. The ion and electron temperatures remain nearly equal in the interior of the foil. For the same initial conditions, if the laser energy is absorbed by inverse bremsstrahlung the maximum density at the peak of the laser pulse is slightly above solid density and back surface is much cooler, about 5 eV. At the end of the laser pulse the density has dropped by almost an order of magnitude below solid density.

Figure 15 shows, in the x-t plane, the evolution of the 1.06 μm critical density (10^{21} cm^{-3}) front surface, $X_{c1.06\ \mu m}$, the .53 μm critical density (4×10^{21} cm^{-3}) back surface, $X_{c.53\ \mu m}$ the maximum density surface, $X_{\rho_{max}}$ and the maximum pressure surface, $X_{p_{max}}$. As shown in Figure 14 the maximum density and pressure vary along $X_{\rho_{max}}$ and $X_{p_{max}}$. The maximum pressure surface is often referred to as the ablation surface. It is significant as an accelerating force only during the laser pulse. It can be seen from this Figure that after the laser pulse, t ~ 3 nsec, the maximum pressure surface is associated with the hot expanding plasma. The motion of the back .53 μm critical surface is studied with a side viewing streak camera.

Figure 16 summarizes the predicted laser intensity, I_L, dependence of the velocities of the rear .53 μm and front 1.06 μm critical surfaces at 2 nsec and 10 nsec respectively. The presence of superthermal electrons affects the magnitude and functional dependence of these velocities on the laser intensity.

The diagnostic instrumentation employed in these experiments is schematically depicted in Figure 17. The focal spot was located by maximizing the intensity of the back reflected laser light incident on a 250 μm diameter spherical ball. The incident laser pulse had a 1 - 3 nsec FWHM Gaussian temporal envelope and was focused on the target by an f/2 lens. The forward scattered laser light was also collected with an f/2 lens. The primary diagnostic was the side viewing, 10 psec resolution, streak camera which measured the temporal evolution of a small region of the front or back surface of the target. The near and far field cameras[13] provided information about the spatial laser beam quality and the focal spot energy distribution in the absence of the laser produced plasma, respectively. The x-ray diagnostics provided time integrated measurements of the x-ray bremsstrahlung emission spectrum for photon energies above 1 keV. This x-ray emission spectrum is related to the electron spectrum inside the target plasma. The electron spectrometer provided information about the high energy (6 - 160 keV) electron distribution and the plasma potential. The x-ray pinhole cameras were operated with a magnification of unity. Each possessed four rows of pinholes whose diameters were: 75 μm, 25 μm, 12 μm, and 6 μm. One row of pinholes was uncovered. The other three rows were covered with thin mylar and aluminum K edge filter combinations to provide spectral information in the 1 - 5 keV x-ray energy range. The side viewing x-ray microscope[14] was used to view the plasma plume. The ion charge collectors were positioned 21 ± .5 cm from the target and were used to measure the symmetry of the ion convective motion and the momentum transfer during the foil acceleration. The transmitted light measurements provided information on the initial formation of the plasma and the temporal and time integrated spatial distribution of the laser light refracted around the target

plasma. During the experiments it was necessary to operate with target chamber pressures of $\leq 10^{-3}$ torr or less in order to avoid electron transit scattering losses to the electron spectrometer and photoionization in the ion charge collectors.

The results from two representative foil acceleration experiments are presented in Figures 18, 19 and 20. The laser pulse irradiation energy and duration (FWHM) were 9.2 J in 1.5 nsec and 20 J in 1.3 nsec, respectively. The target in each experiment was a 10 μm thick polyethylene foil. The peak laser intensity based on far field camera measurements, was approximately 5.1 x 10^{13} W/cm^2 for the 9.2 J shot and 1.3 x 10^{14} W/cm^2 for the 20 J shot. The diameter of the low energy x-ray emission region, inferred from the x-ray pinhole picture of the front surface blow off plasma, was approximately 130 - 150 μm. The diameter of the rear surface low energy x-ray emission region, measured with an x-ray pinhole camera facing the rear surface of the target, is approximately one-half the diameter of the front surface emission region. The transmitted laser energy in the 9.2 J and 20 J experiments was .62 J and .11 J, respectively. This transmitted light occurs prior to and during the initial breakdown and formation of the plasma. The laser energy reflected from the target in the 9.2 J and 20 J experiments was .58 J and 2.3 J, respectively.

Streak photographs of the evolution of a small segment on the back surface of the target are presented in Figure 18. The laser pulse which produced the back surface acceleration, by ablating the front surface of the target, is given to the right of each streak photograph. A different optical image transfer system was used in each experiment. On the 9.2 J experiment time increased from right to left and the field of view was 440 μm. For the 20 J experiment time increased from left to right and the field of view was 1430 μm. The motion of the accelerated plasma away

from the back surface of the target, in each case, proceeds vertically. The target was tilted very slightly producing a mirror image of the accelerated plasma in the streaked photograph due to reflection of the plasma emission light from the surrounding polyethylene foil and target frame.

The streak photograph of the 9.2 J experiment shows the initial movement of the back surface of the target with a velocity of approximately 5 x 10^6 cm/sec. This early motion may be thermal expansion of the back surface plasma produced by excessive heating during the initial foil breakdown and plasma formation process since it corresponds to an average particle thermal energy of several eV. At latter times (~ 2 nsec) the compressed, accelerated plasma becomes much more luminous and overtakes the low density thermal blow-off. Its convective velocity has increased to 1.4 x 10^7 cm/sec and agrees well with the corresponding rear surface velocity calculation results presented in Figure 16 with superthermal electrons present.

The streak photograph of the 20 J experiment shows the late time evolution of the back surface plasma. This photograph shows the plasma convective velocity increasing from 1.3 X 10^7 cm/sec to its asymtotic value of 3.0 x 10^7 cm/sec. This agrees with the asymptotic rear surface velocity measured by the ion time of flight probes; Figure 19. The time of arrival of the peak of the ion charge pulse on the detector located at 156° corresponds to an average velocity of 3.0 x 10^7 cm/sec. The average front to back ion convective energy ratio, measured with the ion collectors

during the 20 J experiment, was 2.9. The anamolous signal which follows the initial ion charge collection signal on the ion detector located at 26° is due to breakdown in the detector and may be disregarded.

The high energy x-ray emission spectra are presented in Figure 20. The x-ray spectra show that the electron energy distribution inside the target is highly non-Maxwellian. The sensitivity of the tail of the x-ray emission spectrum to the laser pulse energy is also evident. The high energy electron emission spectra also exhibited this behavior. Techniques are presently being developed to use these x-ray and electron spectra to obtain information about the plasma potential. Information about the plasma potential is necessary in order to quantitatively relate the x-ray and electron emission spectra.

The preliminary results reported above are typical of those obtained from recent foil acceleration experiments performed using the Long-Path Laser System. The experimental results are in approximate agreement with one dimensional computer calculations when significant production rates for superthermal electrons are included. The high energy x-ray emission measurements are also consistent with this result. These superthermal electrons are produced by resonant and parametric absorption process at the high laser intensities employed in these experiments. The presence of local hot spots in the laser focal spot probably result in enhanced high energy electron production. This nonuniform laser energy distribution at the target prevents detailed comparisons between theory and experiment.

Finally, early time streak measurements indicate that the initial breakdown and heating of the plasma may have an important effect on the foil acceleration process.

A. Ultra Fast X-Ray Streak Camera

The study of laser produced plasmas for fusion application has emphasized the need for a sub-nanosecond resolution detection and recording system sensitive at x-ray wavelengths. Details of the x-ray emission characteristics with time resolution comparable to the plasma heating times will yield data that address the questions of the optical absorption, plasma heating and compression processes. Much present interest is focused on sub-nanosecond optical irradiation of targets, and the concomitant x-ray emission. Unfortunately, nearly all observations of x-ray emission to date have been time integrated because of the absence of suitable time resolved x-ray detectors. Ultrafast streak cameras sensitive in the visible and near infra-red regions of the spectrum have been developed and successfully used in recent years, and the technique is now quite well known.

A unique x-ray streak camera for use with photon energies in the 1 - 10 - keV range has been developed. The temporal resolution of the device is nominally 50 psec. In addition to the high time resolution, a streak camera can provide one degree of spatial resolution. By coupling the streak camera to imaging, dispersing, or filtering elements, time-resolved records of the corresponding distributions can be obtained in a single experiment.

The x-ray-sensitive photocathode of the streak camera is formed by depositing a 100-Å-thick layer of gold on the rear surface of an 5×10^{-3}-mm-thick beryllium vacuum window (45% transmission at 1 keV). The cathode operates in the transmission mode. Gold was chosen as the

photocathode material because it exhibits high quantum efficiency in the photon energy range of interest. For example, measurements have shown a 10⁻³ quantum efficiency with 2.9-keV photons. We have measured the energy distribution of emitted photoelectrons from the gold cathode by an electron spectroscopy technique. These measurements yield a nearly linear distribution in energy out to a maximum electron energy equal to the incident photon energy. This distribution implies that the bulk of emitted photoelectrons are secondaries. The rms electron energy spread is 240 eV. For an average photon energy of 0.3 keV and a photocathode accelerating field of 3500 V/cm, this distribution yields a transit time dispersion just under 50 psec.

Figure 21 is a schematic diagram of the electro-optic x-ray streak camera. The camera tube is a modification of a commercially available spherically focused imaged converter tube (RCA C73435) into which the new cathode-grid assembly was incorporated. The grid behind the photocathode provides a high accelerating field to reduce the transit time dispersion of the photoelectrons. The focused electron beam is then linearly deflected by two plates in the field-free region of the tube. An optically triggered avalanche transistor circuit provides the voltage ramp for the deflection plates with very low trigger-time jitter. The photocathode is a 125 μm x 1 cm slit in the front face of the tube.

As seen in Fig. 21, the streak tube phosphor output is fiber-optic coupled to an image intensifier whose output is in turn lens coupled to photographic film.

The x-ray streak camera has been used in preliminary experiments to observe the emission from an iron target when irradiated by up to 1-J 150-psec full width half-maximum (FWHM) pulse from a neodymium laser.

The duration of the observed x-ray emission is roughly equal to that of the irradiating optical pulse except for a somewhat slower fall time. The incident optical pulse is monitored by a nominal 10-psec optical streak camera with an S-1 photocathode. The streak speed of the x-ray camera has been determined by irradiating the iron target with two 0.5-J pulses separated by 300 psec. This was accomplished, as shown in Fig. 22, with a beam splitter and mirrors so that the incident pulse was divided into two equal intensity pulses that were focused onto closely spaced but not overlapping areas of an iron slab target. The x-ray emission spans roughly the 0.5-1.5-keV range; the average photon energy is about 1 keV. The focal spot diameter in these experiments was approximately 200 μm. As a result of this double irradiation, two plasmas were formed with a creation time separation of 300 psec. The x-ray streak camera recorded the temporal history of the x-ray emission from the two plasmas. Figure 23 is a microdensitometer trace of the streak record with an actual film record shown in the inset. The measured separation of the streaks on the film with the known 300-psec time separation yields a streak speed of 40 psec/mm on the film.

This streak speed provides an estimate of the streak-limited resolution of 12 psec. Combined with the transit time dispersion of 50 psec, the overall time resolution remains at about 50 psec. The well-resolved separation of the pulses in Fig. 23 provides experimental verification for this short time resolution.

Fig. 24 is a recent result showing some filtered x-ray streak data from an iron target. Again two pulses were used, this time 500 psec apart. The filtering at various regions of the streak camera input slit is shown.

Actually the 150 μm Be filtered area is the upper half of the region identified as 25 μm Be. The Be stops the Fe L radiation but passes the K, whereas the Al stops the K also.

We are continuing our x-ray streak camera development toward further applications to time resolved x-ray intensity, spectral, and image data.

B. Interferometry

Figures 25, 26 and 27 describe the experimental set up used in our continuing efforts to develop a high spatial and temporal resolution interferometer appropriate for the study of plasmas produced by sub-nanosecond laser pulses.

Although such things as target environment prior to irradiation, and blowoff symmetry after irradiation must be determined, our primary interest is in the determination of electron density distributions in the vicinity of the critical region during irradiation. Such determinations have a two-fold purpose. First, a knowledge of density scale lengths in the critical region is required to understand the physical process of optical absorbtion. Second, this data can be used as a quantitative check on the hydrodynamic codes currently used to study implosion.

It is clear that measurements of this type require spatial resolutions on the order of a micron, and short probing wavelengths to reduce refractive errors in the subsequent unfolding of data. Fig. 25 shows the manner in which a frequency trioled probe pulse at 3547 Å is obtained. Energy conversions in excess of 30 are regularly obtained (ω to 3ω). In Fig. 26 is shown a holographic microinterferometer capable of providing 1 μm resolution. Finally, Fig. 27 displays a recent result obtained with this setup. The probe pulse duration was approximately 90 pseconds at 3547 Å. Abel inversion of this photograph suggests that the 10^{21} electrons/cc region was clearly resolved.

V. SUMMARY

Several laser systems have been described and experiments relevant to laser produced implosions have been reported.

The target experiments have been designed to provide code-normalization data in a regime of interest to laser fusion. Target masses are chosen to be heated to 1 keV temperatures with the available laser energy ~ 40 J. The laser power density on target (10^{11} W/cm^2 to 10^{15} W/cm^2) has been varied in order to investigate anomalous heating mechanisms as well as instability thresholds. The exact development of plasma gradients as a function of time has been recorded with a holographic interferometer. The interaction of the laser with the target has been recorded with optical streak cameras and conventional photographic techniques. The reflection, transmission, and refraction of the incident laser pulse from the plasma target have been measured. The target temperature was determined by measuring the time integrated and time resolved x-ray emissions. X-ray emission as a function of time was measured with fast diodes and with a newly developed x-ray streak camera. The target x-ray emission was measured absolutely from ~ 1 keV to ~ 150 keV. This data is used to determine the electron energy distribution.

REFERENCES

1. The amplifier design has been extensively described in the Laser Fusion Semi-Annual Reports, UCRL 50021-73-1 and UCRL 50021-73-2.

2. J. E. Swain, R. E. Kidder, K. Pettipiece, F. Rainer, E. D. Baird, and B. Loth, J. Appl. Phys., 40, 3973 (1969).

3. L. W. Coleman, J. E. Swain, F. Rainer, and R. A. Saroyan, "Pulse Characterization for the Long-Path Laser at LLL", UCRL 74626 (1973).

4. R. Allyn Saroyan, "Laser Intensity Measurement", UCID 16550 (1974).

5. A. J. DeMaria, W. H. Glenn, Jr., M. J. Brienza, and M, E. Mack, "Picosecond Laser Pulses," Proc. IEEE 57, 2-25 (Jan. 1969).

   Ya.B. Zel'dovich and T. I. Kuznetzova, "Generation of Ultrashort Light Pulses by Means of Laser." Sov. Phys. Uspekhi 15, 25-44 (July 1972).

6. D. J. Kuizenga and A. E. Siegman, "FM and AM Mode-Locking of the Homogeneous Laser - Part I and Part II," IEEE J. of Quant. Electron. QE-6, 694-715 (Nov. 1970).

   D. J. Kuizenga, D. W. Phillion, T. Lund, and A. E. Siegman, "Simultaneous Q-Switching and Mode-Locking in the cw Nd:YAG Laser," Optics Comm. 9, 221 (Nov. 1973).

7. Calculation of G. W. Leppelmeier:

   $$Q = \sqrt{\pi}\,\frac{E\,a^2\,A\,e^{\alpha L}}{16\,f^2\,\alpha^2 L}$$ = Joules stopped by target

   E = effective stored energy density in J/M^3, $e^{\alpha L}$ = gain

   a = target diameter in M, f = focal length of lens in M

   A = lens area - M^2, L = length of gain media M), α = effective gain M^{-1}.

8. N. Bloembergen, "Laser Induced Electronic Breakdown in Solids," IEEE J. Quant. Electron. QE-10, 375-386 (March 1974).

   See articles by G. W. Leppelmeier and B. Newnam in "Laser Induced Damage in Optical Materials 1974," A. J. Glass and A. H. Guenther eds., NBS Special Publication, U. S. Gov. Print Office, Washington, D. C., 1974, to be published.

9. J. H. Nuckolls, G. H. Dahlbacka, J. D. Lindl, W. C. Mead, H. D. Shay, A. R. Thiessen, G. B. Zimmerman, Semi-Annual Report - July-December, 1973, UCRL 50021-73-2, 69, (1973).

10. W. C. Mead and J. D. Lindl, "Two-Dimensional Simulation of Hydrodynamic Instability in Laser Fusion Implosions," UCRL 75077, (1974).

11. G. B. Zimmerman, "Numerical Simulation of the High Density Approach to Laser Fusion," UCRL 75173, (1973).

12. H. D. Shay, C. Bailey, S. Bodner, J. Katz, W. Kruer, J. Nuckolls, W. Slivinsky, E. Valeo, and G. Zimmerman, "Superthermal Electron Distributions in Laser-Produced Plasmas," UCRL 75465, (1974).

13. R. Allyn Sarayan, "Laser Intensity Measurements," UCID 16550, (1974).

14. F. D. Seward and T. M. Palmieri, "A Simple X-Ray Microscope for Photographing Laser-Produced Plasmas," UCRL 75799, (1974).

FIGURE CAPTIONS

1. Schematic diagram of JANUS
2. Photograph of JANUS with target area in the rear
3. Optical diagnostic set up for JANUS
4. JANUS target chamber being readied for target studies
5. Photograph of Valkyrie with oscillator in the rear
6. Photograph of Valkyrie target area
7. Long-Path Laser target area
8. A typical laser fusion target which consists of a hollow glass shell 74 μm in outside diameter is shown
9. Damage caused in a hollow glass ball by a focused mJ laser pulse
10. Diagram of the experimental set-up used to study the prepulse characteristics of the JANUS Oscillator
11. Typical experimental records from the prepulse experiments shown in figure 10
12. Streak camera record of the target breakdown
13. Microdot target
14. Numerical simulation of foil acceleration
15. x-t diagram of foil acceleration
16. Laser intensity dependence of surface velocities
17. Foil acceleration experiment diagnostic configuration
18. Foil acceleration streak record
19. Ion emission angular distribution
20. X-Ray Spectra

JANUS LASER SYSTEM

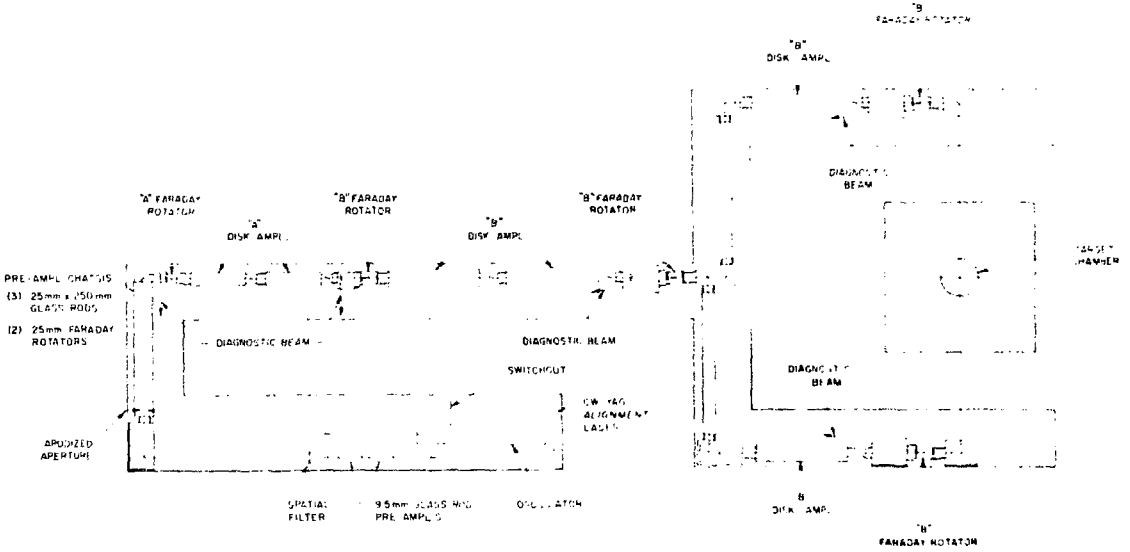

FIGURE 1

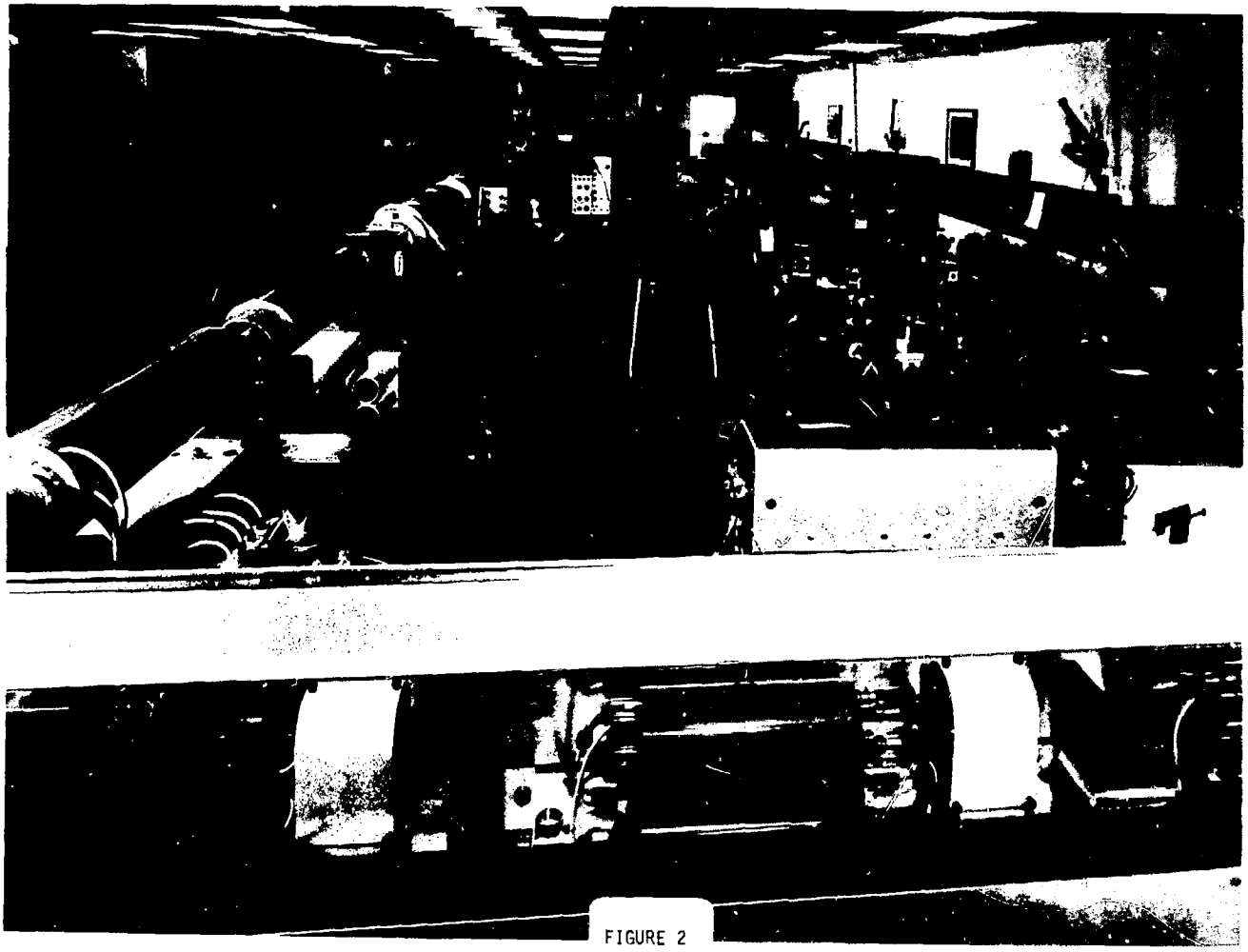

FIGURE 2

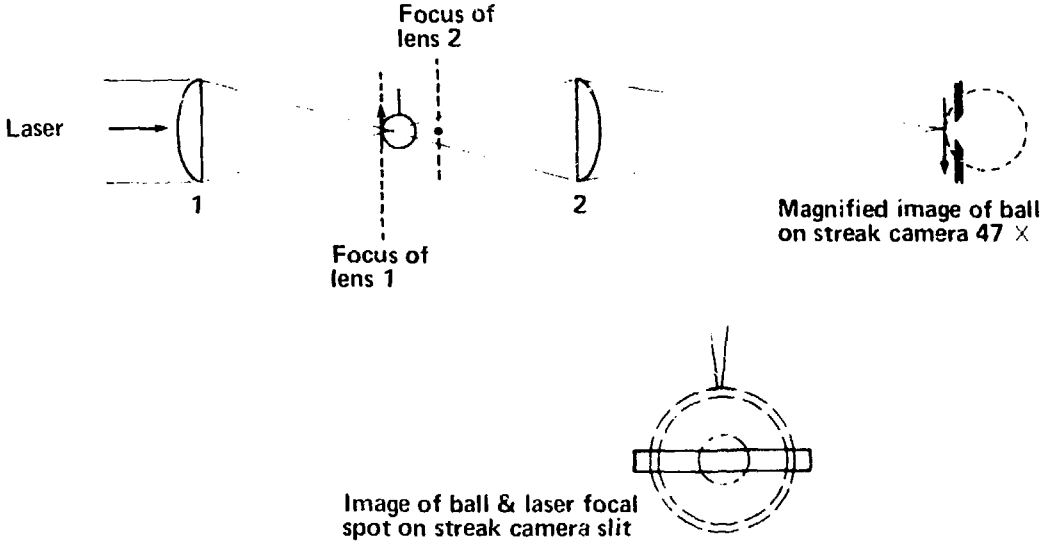
Focus of
lens 2
Laser
1
2
Focus of
lens 1
Magnified image of ball
on streak camera 47 ×
Image of ball & laser focal
spot on streak camera slit

FIGURE 3

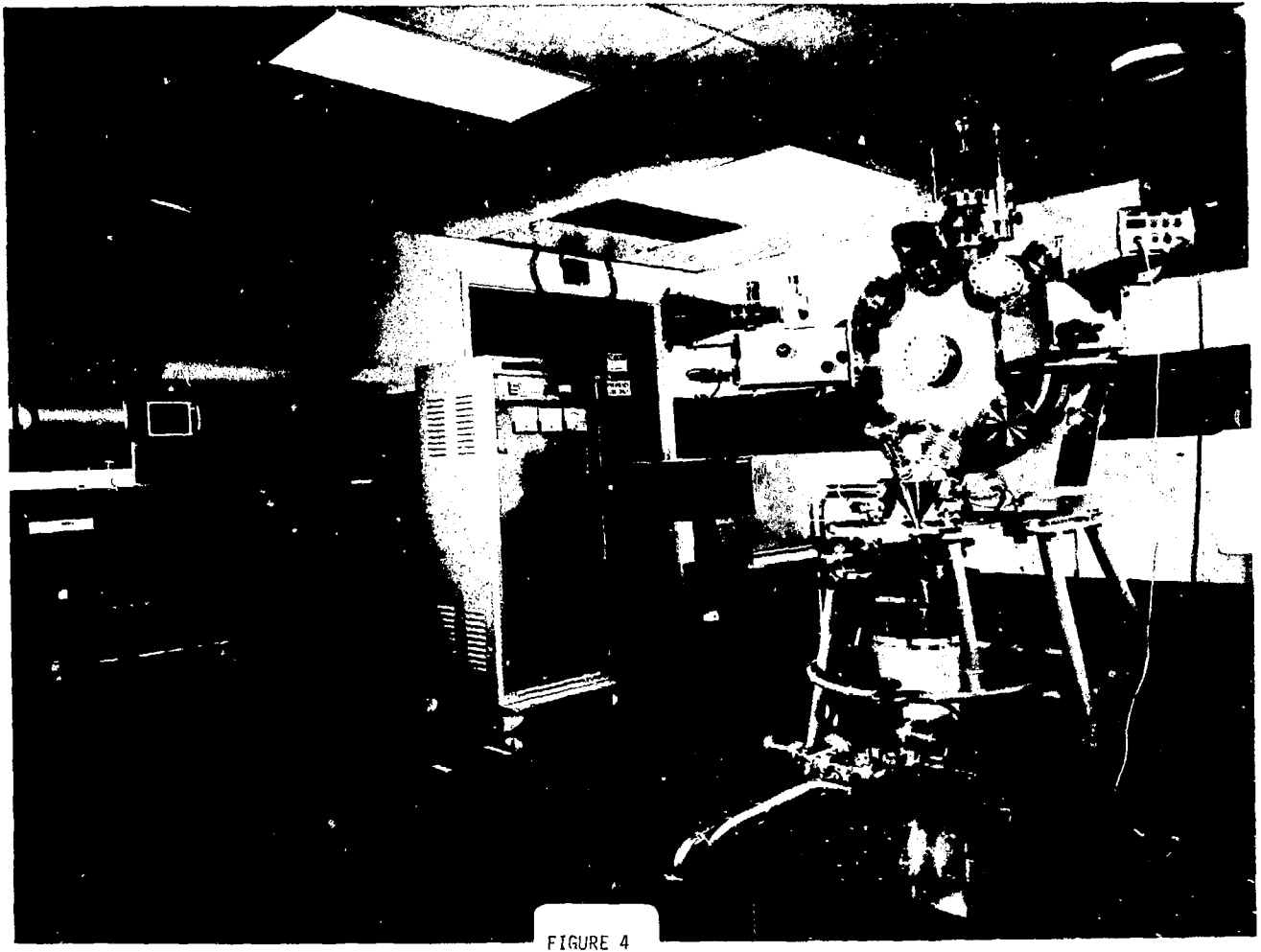

FIGURE 4

FIGURE 5

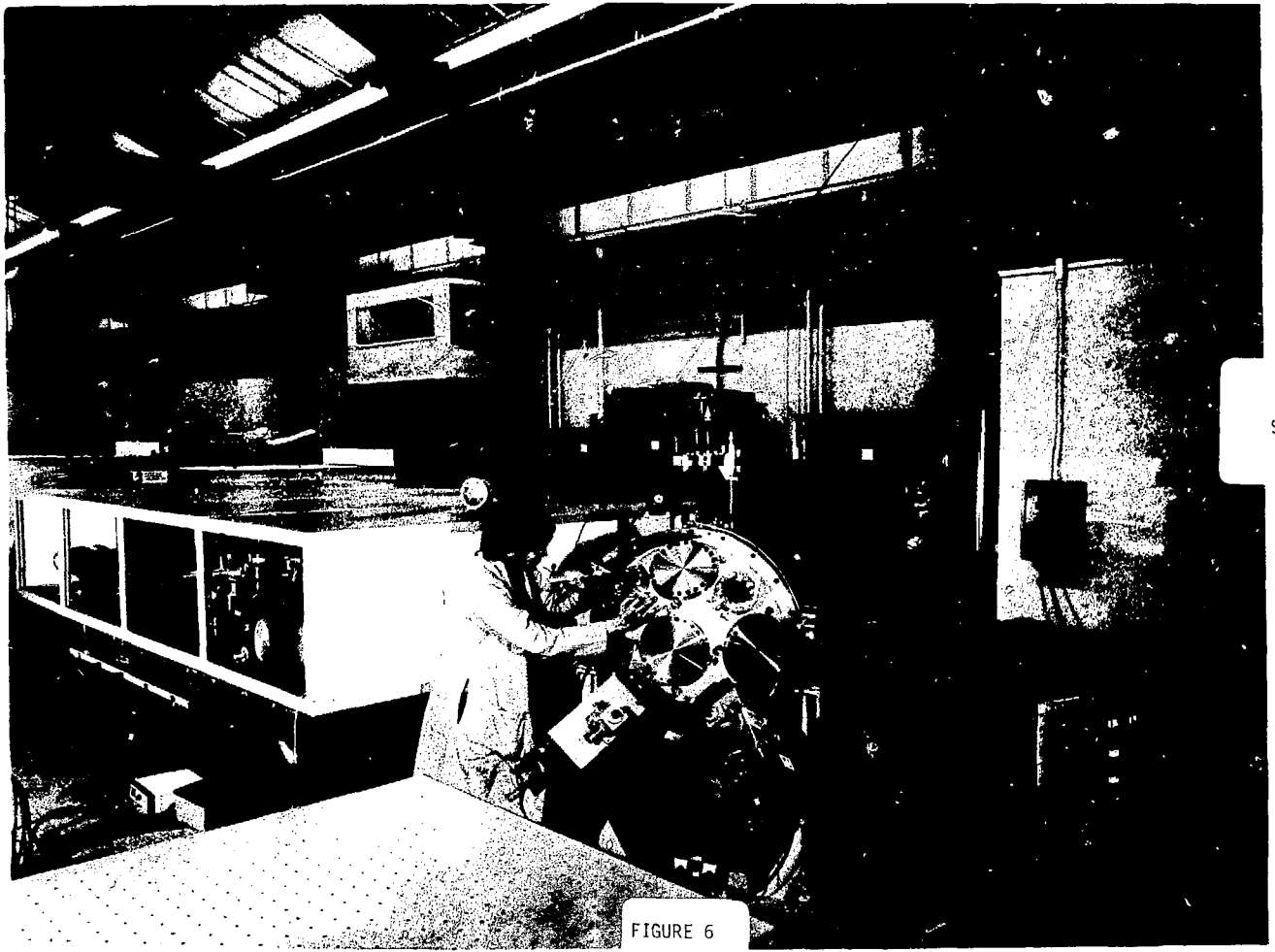

FIGURE 6

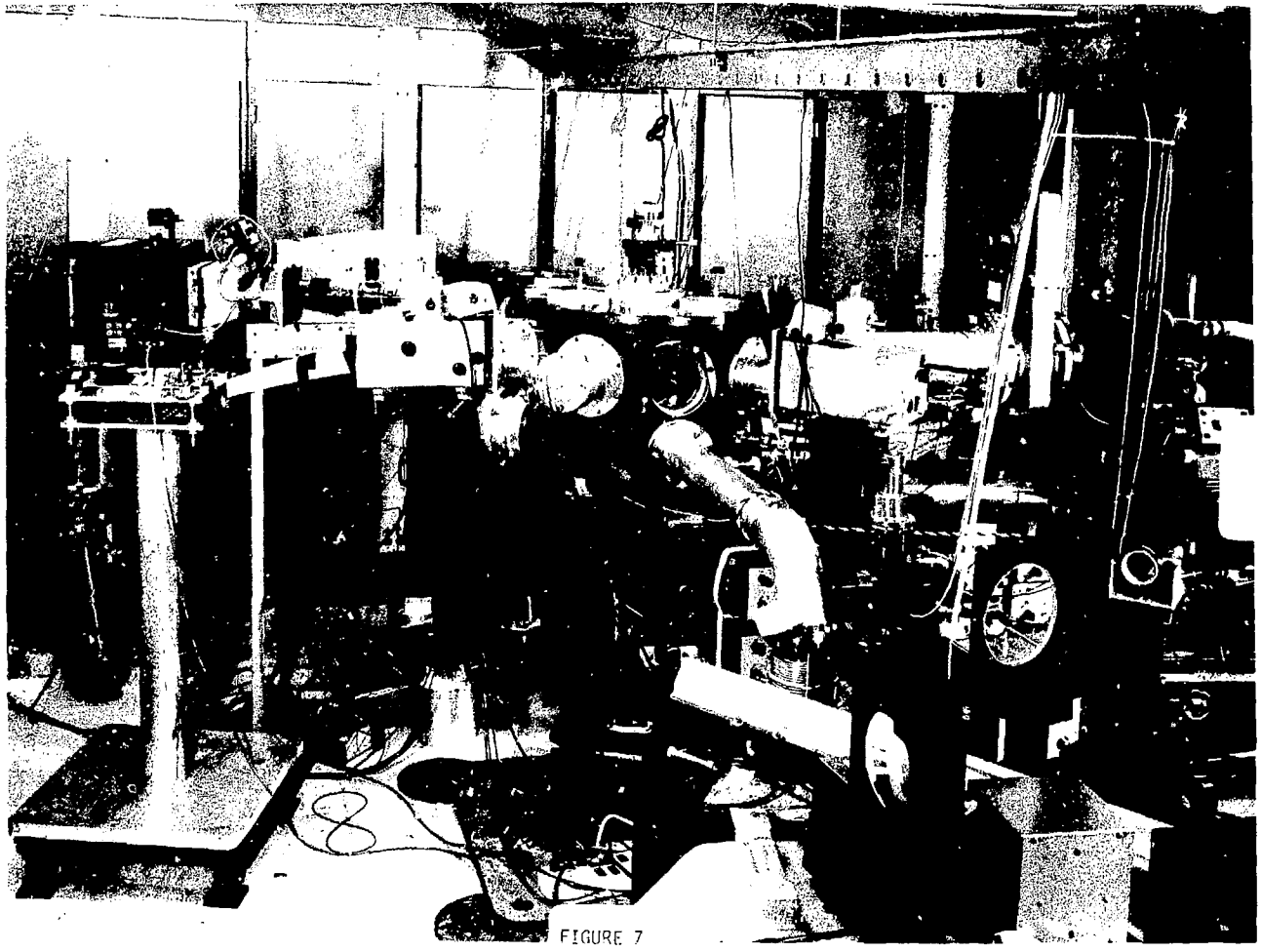

FIGURE 7

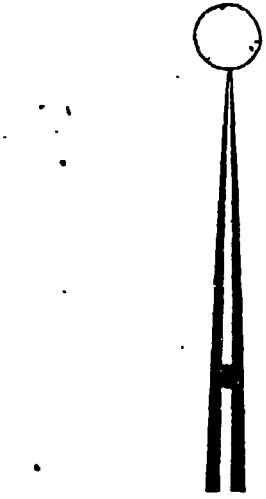

128 X

FIGURE 8

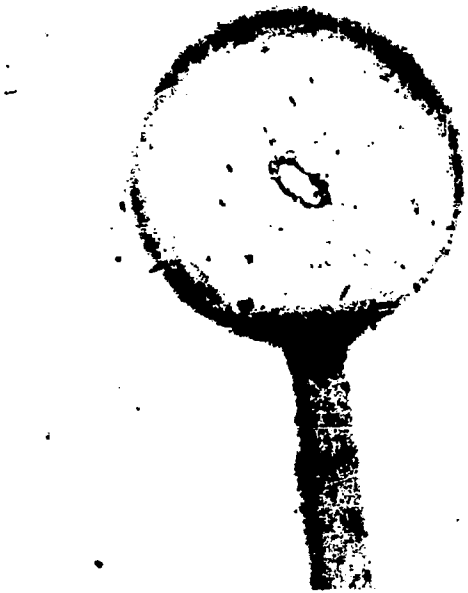

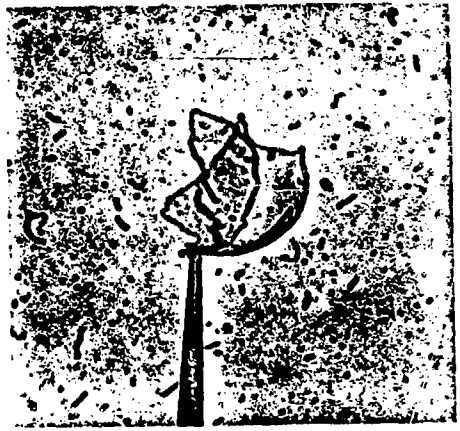

128 X

208 X

FIGURE 9

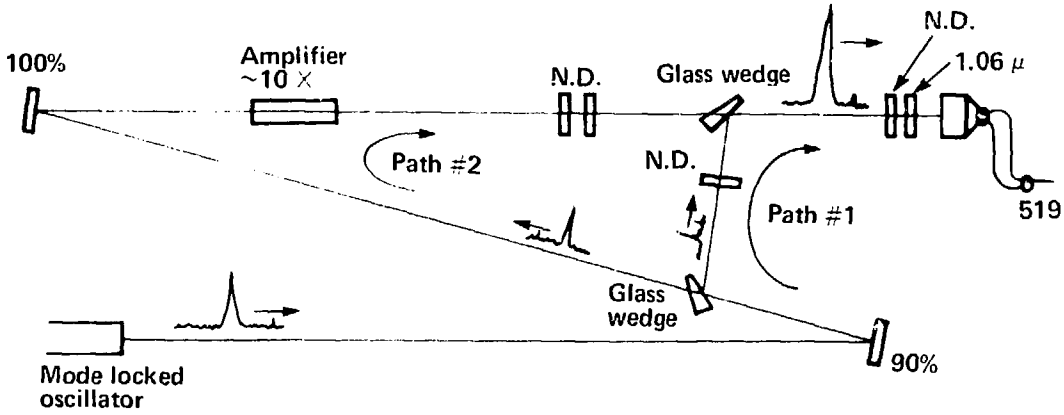
100%
Amplifier
~10 X
N.D.
Glass wedge
N.D.
1.06 μ
Path #2
N.D.
Path #1
519
Glass
wedge
90%
Mode locked
oscillator

FIGURE 10

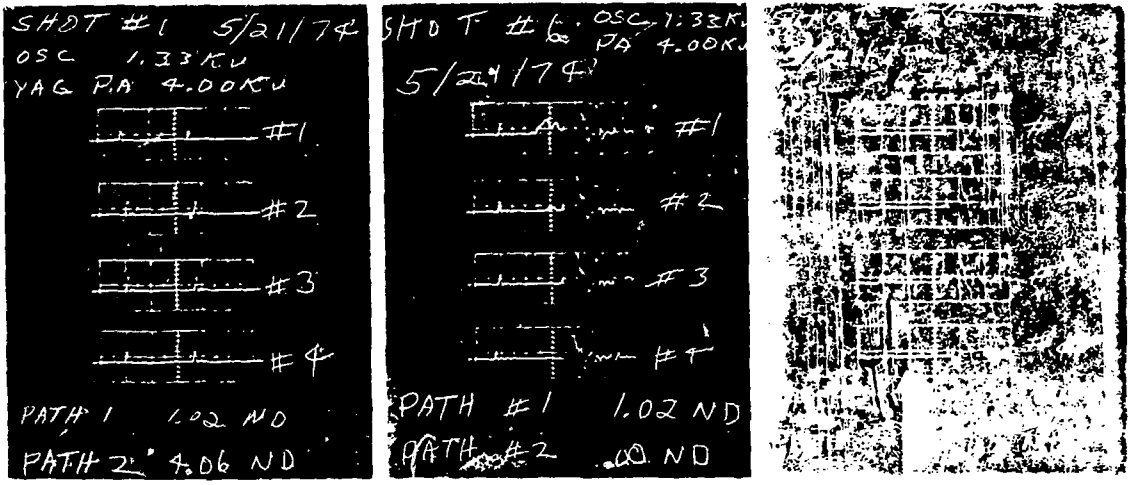

Timing **Noise pulse** **Rejected pulse**

FIGURE 11

TARGET BREAKDOWN

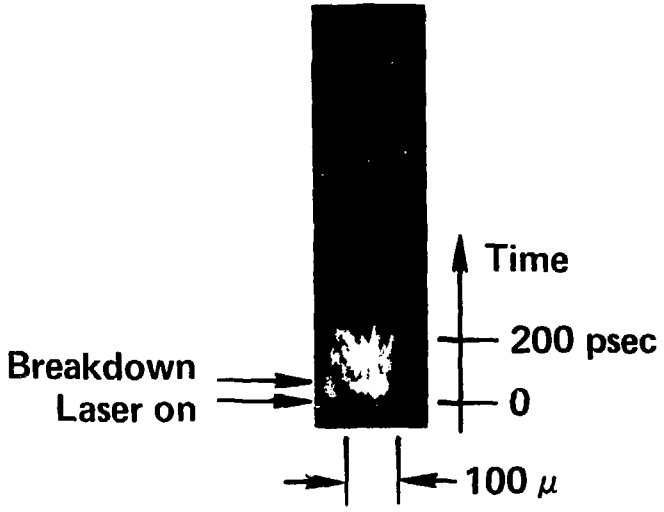

FIGURE 12

TARGETS

I. Polyethylene foils (5–25 μm thick)

II. Polyethylene μdots on 500Å parylene foils

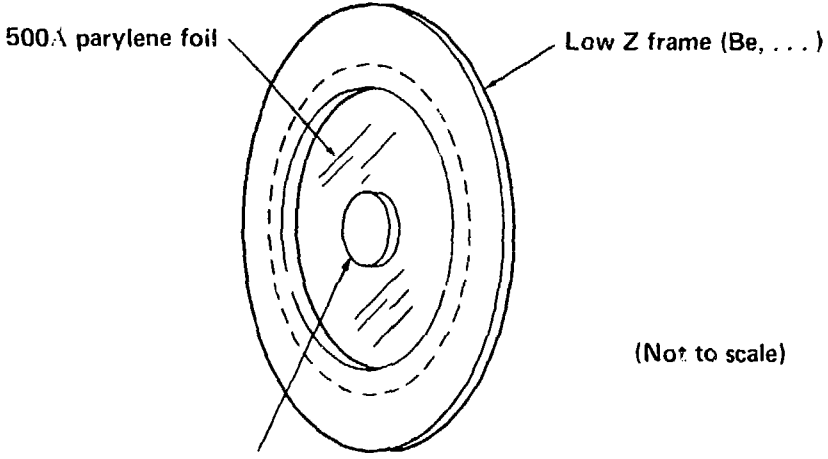

μdot surface tolerance: $x_0 < 100$Å for perturbations with wavelength equal to $\Delta x/2$.

FIGURE 13

1.06 μm, 25J, 1.4 nsec FWHM Gaussian
200 μm dia focal spot, 10 μm thick CH_2 foil (0.83 gm/cm^3)
T_e (keV), ρ (gm/cm^3)

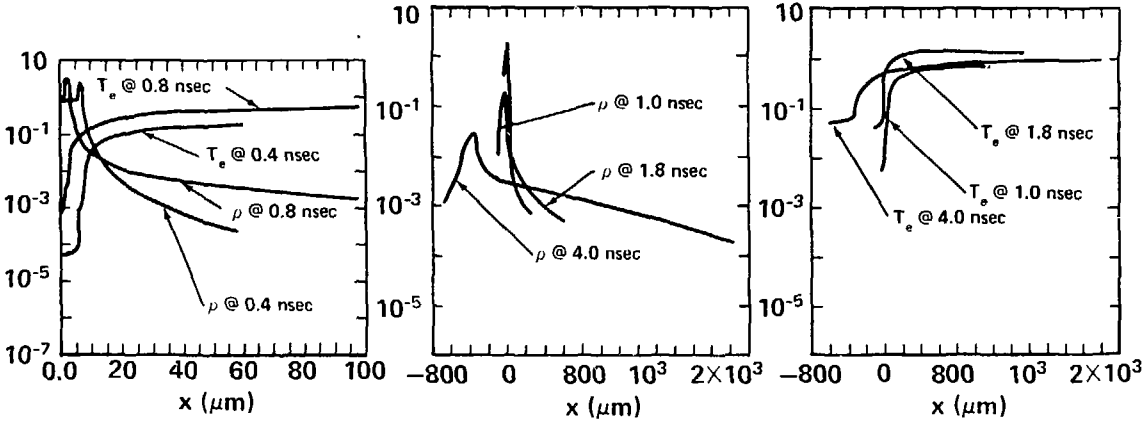

FIGURE 14

x-t DIAGRAM OF FOIL ACCELERATION

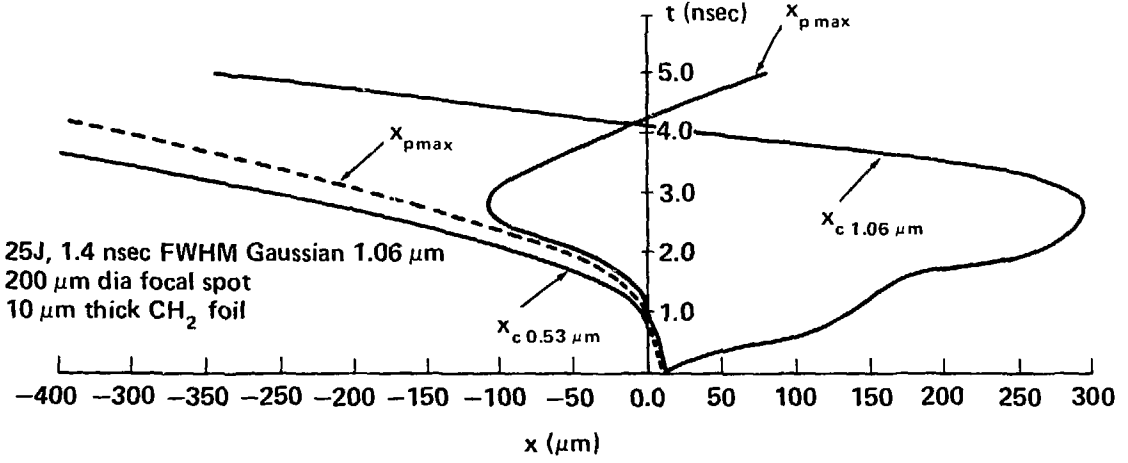

FIGURE 15

LASER INTENSITY DEPENDENCE OF SURFACE VELOCITIES

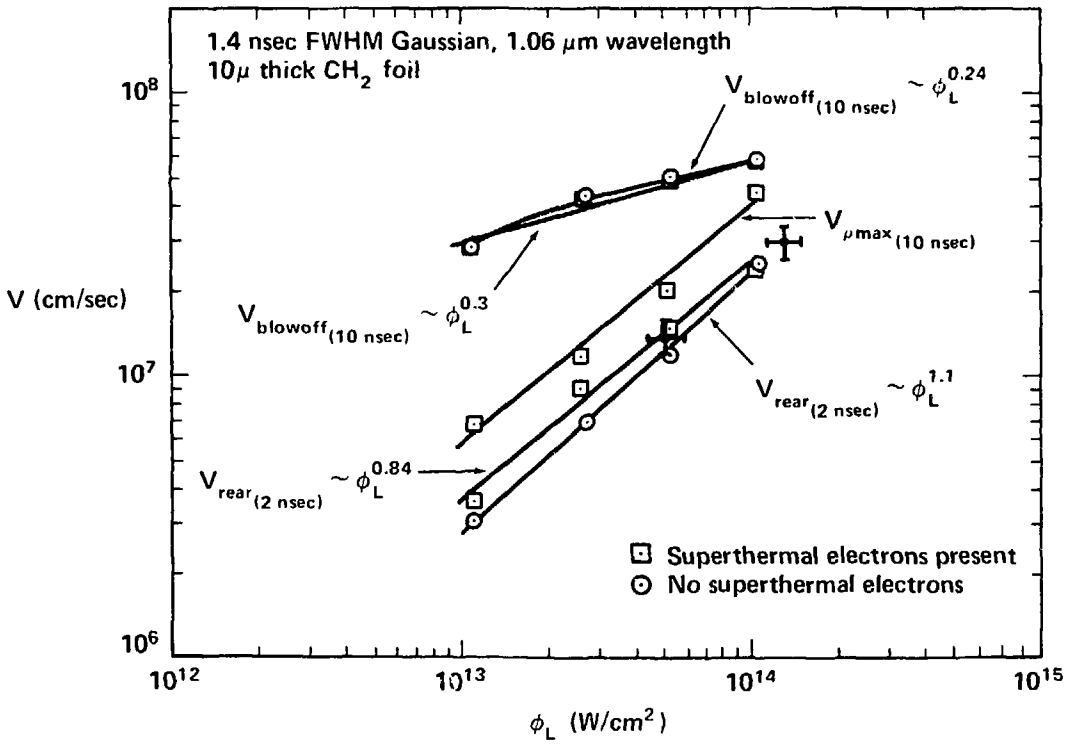

FIGURE 16

FOIL ACCELERATION EXPERIMENT DIAGNOSTICS CONFIGURATION (EQUITORIAL PLANE)

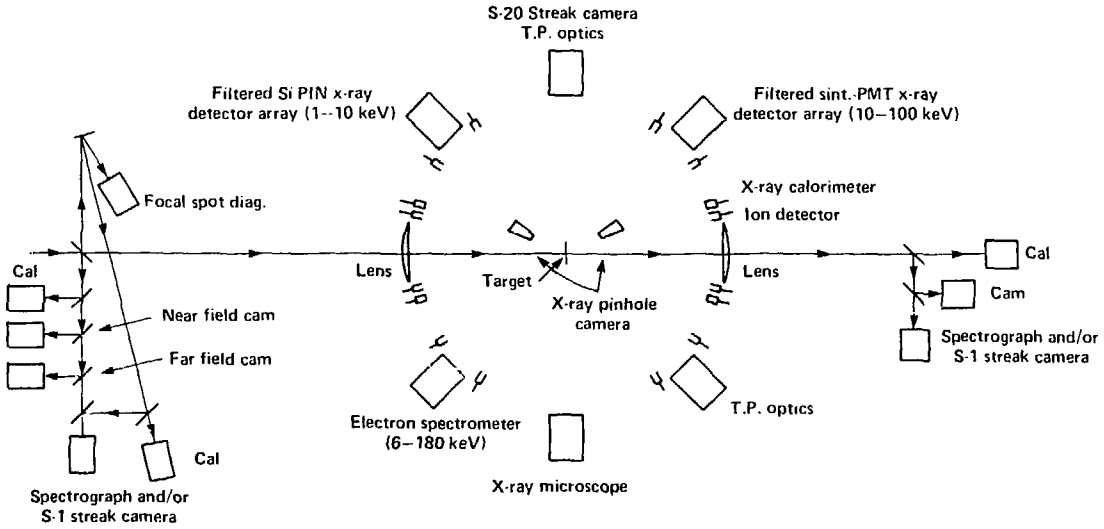

FIGURE 17

Foil acceleration streak photographs

Target surface
(2.4 nsec sweep, mag. 90)

Target surface
(2.4 nsec sweep, mag. 28)

Laser pulse shape

9.2 J, 1.5 nsec FWHM

20 J, 1.3 nsec FWHM

FIGURE 18

ION EMISSION ANGULAR DISTRIBUTION

20 J, 1.3 nsec FWHM, 10 μm thick polyethylene foil

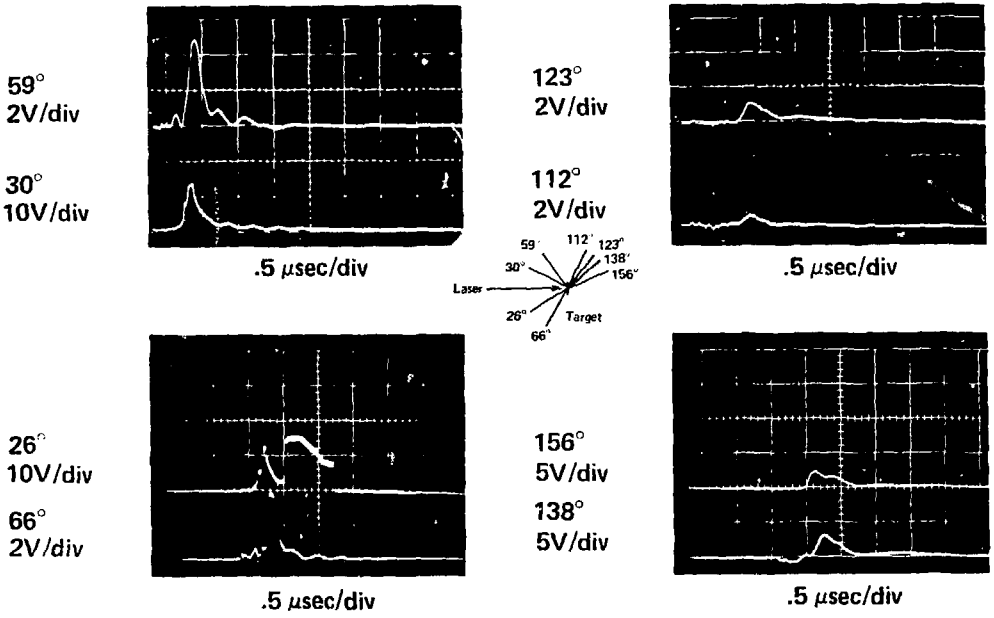

FIGURE 19

X-RAY SPECTRA

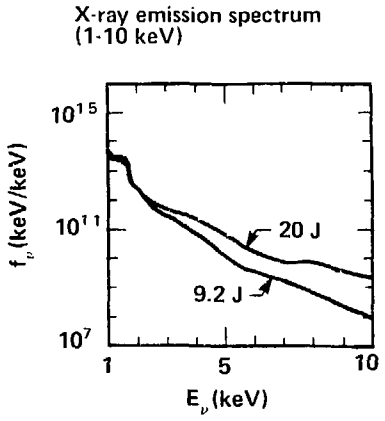

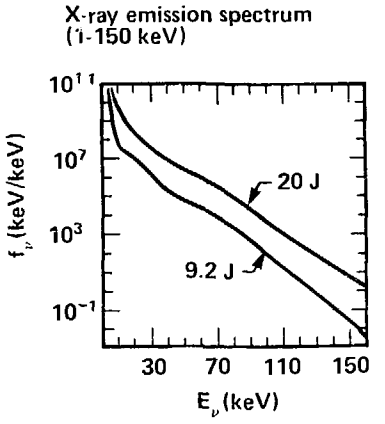

FIGURE 20

X-RAY STREAK CAMERA

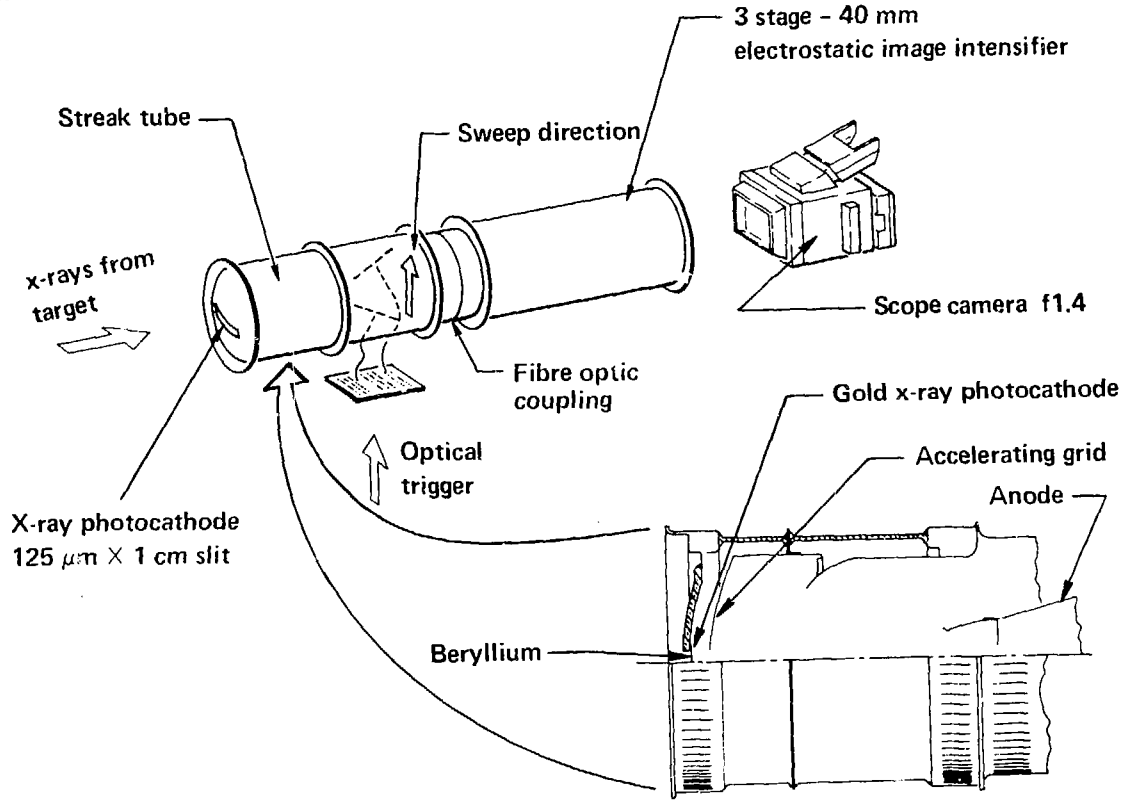

FIGURE 21

DOUBLE PULSE TARGET IRRADIATION

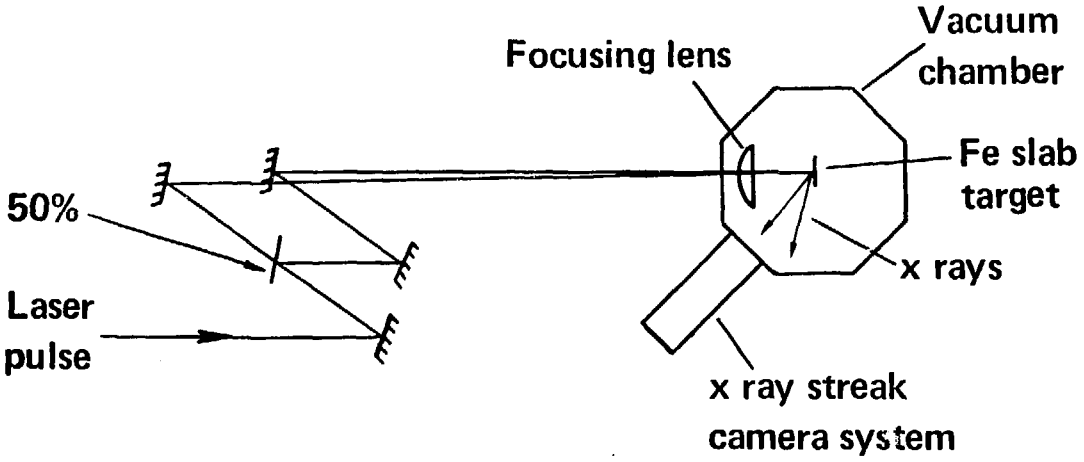

FIGURE 22

DOUBLE X-RAY PULSE

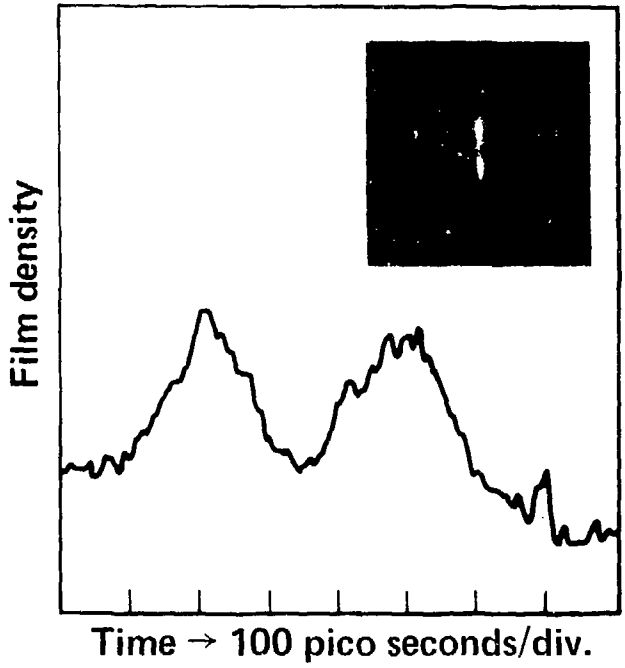

FIGURE 23

DOUBLE PULSE X-RAY STREAK

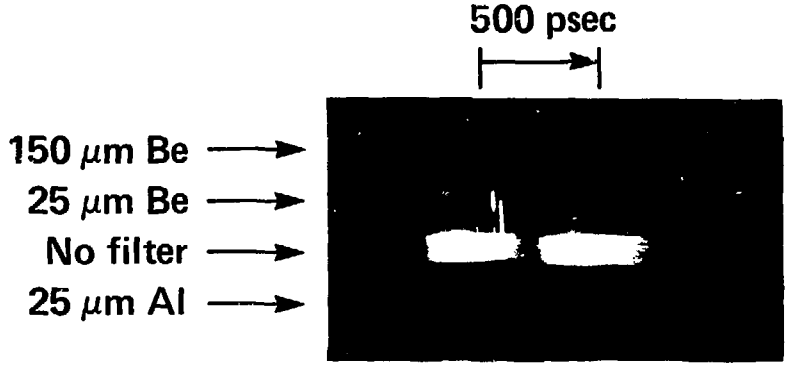

Fe target
Nd laser
0.4 joules/pulse
150 psec pulses

FIGURE 24

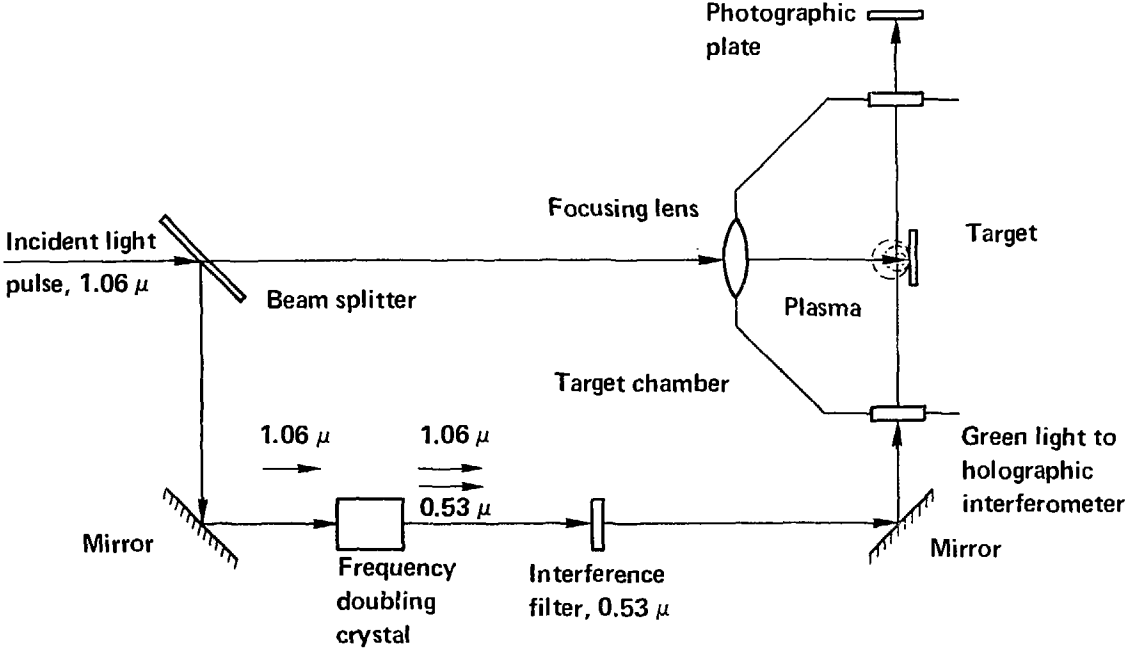
Photographic plate
Focusing lens
Target
Incident light pulse, 1.06 μ
Beam splitter
Plasma
Target chamber
1.06 μ
1.06 μ
0.53 μ
Green light to holographic interferometer
Mirror
Frequency doubling crystal
Interference filter, 0.53 μ
Mirror

FIGURE 25

HIGH RESOLUTION HOLOGRAPHIC INTERFEROMETER

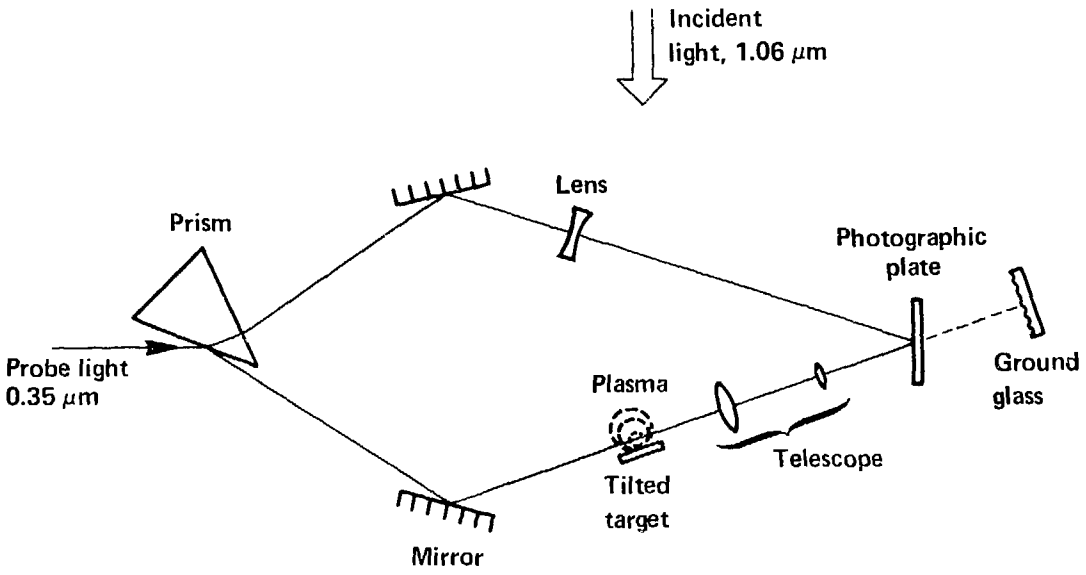

FIGURE 26

3547 Å INTERFEROMETER

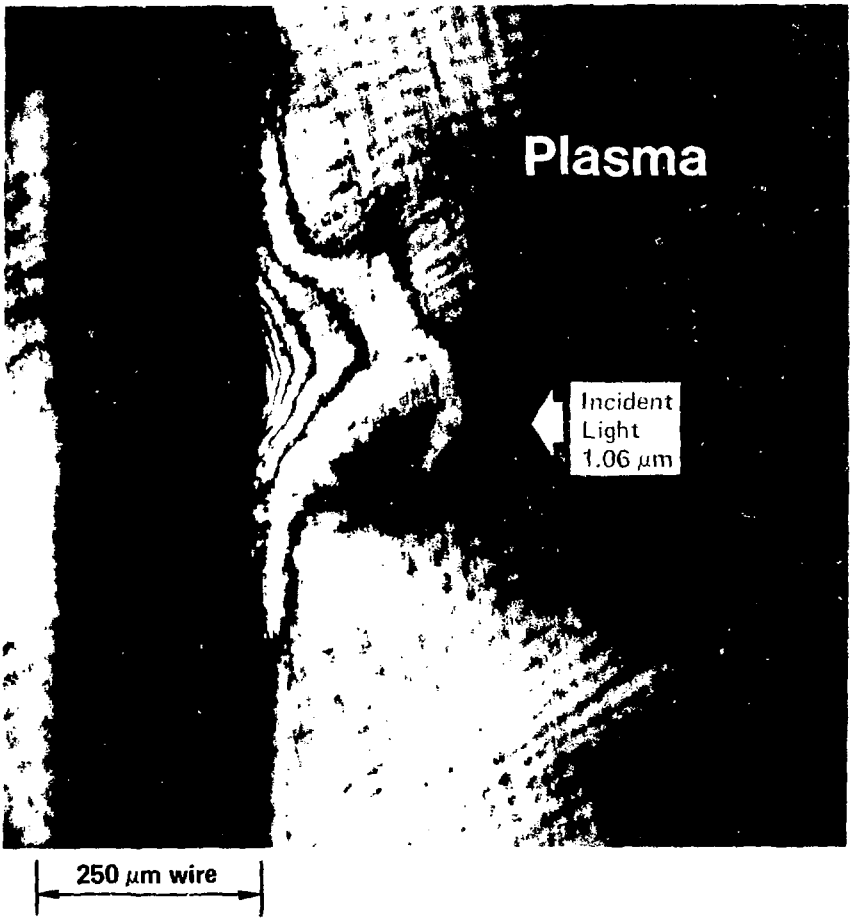

FIGURE 27